Mechanism of near-field Raman enhancement in two-dimensional systems

Rodolfo V. Maximiano,[1] Ryan Beams,[2] Lukas Novotny,[2] Ado Jorio,[1] and Luiz Gustavo Cançado[1,*]
[1]*Departamento de Física, Universidade Federal de Minas Gerais, Belo Horizonte, Minas Gerais 30123-970, Brazil*
[2]*The Institute of Optics, University of Rochester, Rochester, New York 14627, USA*
(Received 1 March 2012; revised manuscript received 25 May 2012; published 18 June 2012)

A theory describing the near-field Raman enhancement in two-dimensional (2D) systems is presented. The analysis quantifies the near-field Raman intensity as a function of the tip-sample distance, Raman polarizability tensor components, incident laser beam configuration, and tip orientation relative to the sample plane. Our results show that the near-field Raman intensity is inversely proportional to the 10th and 8th power of the tip-sample distance in the incoherent and coherent scattering regimes, respectively. Optimal conditions for the tip inclination angle for different configurations are determined, and the results can be used as a guide for tip-enhanced Raman spectroscopy (TERS) experiments in 2D systems such as graphene, two-dimensional electron gases, and topological insulators.

DOI: 10.1103/PhysRevB.85.235434 PACS number(s): 68.37.Uv, 78.30.Na

I. INTRODUCTION

The recent production of micron-sized graphene crystals has triggered a new era in materials science.[1–3] Starting from graphene itself, its conduction electrons present linear dispersion, thereby providing a prototype for the study of relativistic massless Fermions.[1,2] Other unusual phenomena such as fractional quantum Hall effect and ultrahigh mobility at room temperature have established graphene as one of the most studied materials in current research.[4–6] In the field of nanoelectronics, although graphene presents outstanding properties for the production of analog high-frequency transistors,[7,8] the lack of electronic bandgap hampers its application on the production of dc digital transistors.[9] In order to explore alternative routes, scientists are now producing hundreds of other types of two-dimensional materials obtained from the exfoliation of layered compounds such as transition-metal dichalcogenides, transition oxides, and boron nitride (BN).[3,10] In this new wave, the production of operational dc transistors made by single-layer molybdenum disulfide (MoS_2) have been recently reported.[11]

Raman spectroscopy is one of the main techniques used to characterize graphene, and has also been applied to the study of other types of atomically thin films such as MoS_2 and BN.[10,12,13] However, in order to investigate nanosized features in these systems such as point defects and local strain,[14–17] optical techniques like Raman spectroscopy present a strong restriction due to the relatively low spatial resolution caused by diffraction. Tip-enhanced Raman spectroscopy (TERS) provides an opportunity to go beyond this limit, making it possible to achieve spatial resolutions on the order of 100 times smaller than the wavelength of the excitation light.[18–24] For that, a metal tip is positioned a few nanometers above the sample's surface. The tip acts as an optical antenna that generates strongly enhanced near fields at the tip apex.[18,19] The spatial resolution is then determined by the tip diameter, and a recent work has reported TERS measurements in graphene with 20 nm spatial resolution.[25]

Recently, we developed a theoretical analysis for the near-field Raman enhancement in one-dimensional (1D) systems.[26] In this paper, we extend the theory for describing the mechanism of TERS in 2D systems. Our analysis yields the intensity of the near-field Raman scattering as a function of the tip-sample distance and Raman polarizability tensor components. The model accounts for different laser beam configurations and for different tip orientations relative to the sample plane. The analysis takes into account both spatially incoherent and coherent scattering regimes and the results show that, while in the incoherent case the intensity is proportional to the 10th power of the tip-sample distance (in agreement with previous calculations[24,27]), in the coherent case it goes with the 8th power. We applied the results for vibrational modes that give rise to Raman features in hexagonal systems such as graphene and BN. The optimal geometrical conditions are determined, and the results can be used as a guide for TERS experiments performed in 2D materials. Quantitative analysis based on parameters obtained from previous TERS experiments in 1D systems indicates that spatially localized features in 2D systems such as point defects and local strain can generate a signal strength in TERS experiments which is comparable to the strength of the far-field signal obtained from the whole focus area.

II. STATEMENT OF THE PROBLEM AND THEORETICAL BASIS

Figure 1 shows the geometrical configuration of a TERS experiment performed in a 2D system. The field enhancement is obtained from a sharp gold tip acting as an optical antenna. The sample is located at the x-y plane, and the tip position is determined by the tip-sample distance Δ (measured along z), the inclination angle θ, and the azimuthal angle ϕ. The electric field near the gold tip interacts locally with the 2D structure at the laser's frequency ω, inducing a Raman dipole (per square length) located at $\mathbf{r}'$ given by

$$\mathbf{p}(\mathbf{r}',\omega_s) = \overleftrightarrow{\boldsymbol{\alpha}}^{R}(\mathbf{r}';\omega_s,\omega)\,\mathbf{E}(\mathbf{r}';\omega), \tag{1}$$

where $\overleftrightarrow{\boldsymbol{\alpha}}^{R}(\mathbf{r}';\omega_s,\omega)$ is the Raman polarizability (per unit square length), $\mathbf{E}(\mathbf{r}';\omega)$ is the total electric field interacting with the sample at $\mathbf{r}'$ in the sample structure, and ω_s is the frequency of the scattered field. The general Raman polarizability tensor

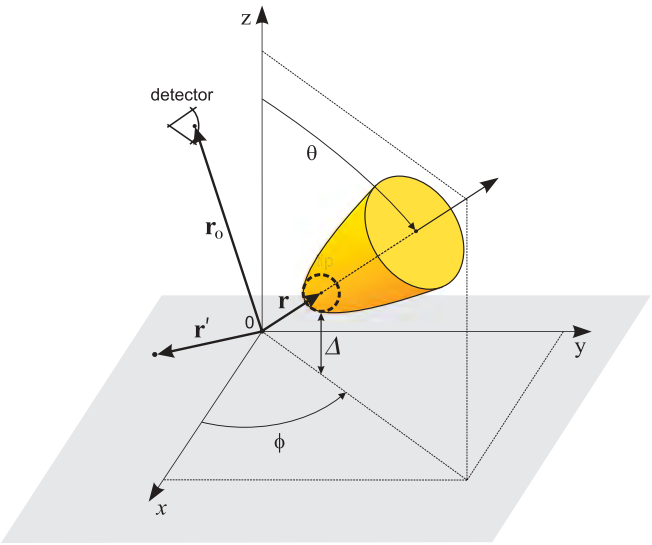

FIG. 1. (Color online) Schematics for TERS experiment performed in a 2D object. The gray area determines the sample plane. The position vectors $\mathbf{r}$, $\mathbf{r}'$, and $\mathbf{r}_o$ denote the location of the center of the tip apex, the Raman dipole moment $\mathbf{p}$, and the detector, respectively. The dashed circumference represents a small sphere of radius ρ_{tip} centered at the tip apex, and Δ is the vertical distance between the tip and the 2D structure.

$\overleftrightarrow{\boldsymbol{\alpha}}^{R}(\mathbf{r}';\omega_s,\omega)$ is represented as

$$\overleftrightarrow{\boldsymbol{\alpha}}^{R}(\mathbf{r}';\omega_s,\omega)=\begin{bmatrix}\alpha_{11} & \alpha_{12} & \alpha_{13}\\ \alpha_{21} & \alpha_{22} & \alpha_{23}\\ \alpha_{31} & \alpha_{32} & \alpha_{33}\end{bmatrix}. \tag{2}$$

We consider here only in-plane Raman modes for which, adhering to the Cartesian coordinates defined in Fig. 1, all matrix elements α_{nm} with n or m equals to 3 are null.

The field $\mathbf{E}(\mathbf{r}';\omega)$ in Eq. (1) is the sum of the laser-irradiated field $\mathbf{E}^{\circ}(\mathbf{r}';\omega)$ and a secondary field generated by induced polarization currents in the tip. At the tip apex, the incident laser field can be written as

$$\mathbf{E}^{o}(\mathbf{r},\omega)=E^{o}_{\parallel}(\mathbf{r},\omega)\,(\cos\beta\,\hat{\mathbf{x}}+\sin\beta\,\hat{\mathbf{y}})+E^{o}_{\perp}(\mathbf{r},\omega)\,\hat{\mathbf{z}}, \tag{3}$$

where $E^{o}_{\parallel}(\mathbf{r},\omega)$ and $E^{o}_{\perp}(\mathbf{r},\omega)$ are the amplitudes of the field components parallel and perpendicular to the sample surface, respectively, and $\hat{\mathbf{x}}$, $\hat{\mathbf{y}}$, and $\hat{\mathbf{z}}$ are the unit vectors in x, y, and z, respectively. β is the angle between the parallel component of the incident field and x. In Eq. (3) we made use of the axial symmetry of the tip.

In a first approximation, the secondary field resembles the field of a point dipole located at the center of a small sphere of radius ρ_{tip} centered at $\mathbf{r}$ (dashed circle in Fig. 1). This dipole moment is defined as[28]

$$\boldsymbol{\mu}(\mathbf{r},\omega)=\overleftrightarrow{\boldsymbol{\alpha}}_{tip}\;\mathbf{E}^{o}(\mathbf{r},\omega), \tag{4}$$

where $\overleftrightarrow{\boldsymbol{\alpha}}_{tip}$ is the tip polarizability. In the case where the tip is oriented along z ($\theta=0$ in Fig. 1), its polarizability tensor assumes the form

$$\overleftrightarrow{\boldsymbol{\alpha}}_{tip}(\omega)=4\pi\varepsilon_o\rho^3_{tip}\begin{bmatrix}(\varepsilon-1)/(\varepsilon+2) & 0 & 0\\ 0 & (\varepsilon-1)/(\varepsilon+2) & 0\\ 0 & 0 & f_e(\omega)/2\end{bmatrix}, \tag{5}$$

where ε_o is the vacuum permittivity and $f_e(\omega)$ is the complex field enhancement factor.[26] The transverse polarizability components correspond to the quasistatic polarizability of a small sphere (dashed circumference in Fig. 1) of radius ρ_{tip} and dielectric constant ε. We assume that the polarizability of the metal tip is much stronger along its shaft, that is, $f_e \gg (\varepsilon-1)/(\varepsilon+2)$. Within this approximation, the polarizability of a tip with the generic orientation shown in Fig. 1 can be obtained by performing a geometrical transformation on the tensor $\overleftrightarrow{\boldsymbol{\alpha}}_{tip}(\omega)$ given in Eq. (5), and the result is

$$\overleftrightarrow{\boldsymbol{\alpha}}_{tip}(\omega)=2\pi\varepsilon_o\rho^3_{tip}f_e(\omega)\times\begin{bmatrix}\cos^2\phi\sin^2\theta & \cos\phi\sin\phi\sin^2\theta & \cos\phi\cos\theta\sin\theta\\ \cos\phi\sin\phi\sin^2\theta & \sin^2\phi\sin^2\theta & \sin\phi\cos\theta\sin\theta\\ \cos\phi\cos\theta\sin\theta & \sin\phi\cos\theta\sin\theta & \cos^2\theta\end{bmatrix}. \tag{6}$$

The dipole moment of a tip oriented according to Fig. 1 can now be obtained by substitution of Eqs. (3) and (6) in Eq. (4), which yields

$$\boldsymbol{\mu}(\mathbf{r},\omega)=2\pi\varepsilon_o r^3_{tip}f_e(\omega)(\mu_x\hat{\mathbf{x}}+\mu_y\hat{\mathbf{y}}+\mu_z\hat{\mathbf{z}}), \tag{7}$$

where the components μ_x, μ_y, and μ_z are given as

$$\mu_x=(\cos^2\phi\sin^2\theta\cos\beta+\cos\phi\sin\phi\sin^2\theta\sin\beta)\,E^{o}_{\parallel}+\cos\phi\cos\theta\sin\theta\,E^{o}_{\perp}, \tag{8}$$

$$\mu_y=(\cos\phi\sin\phi\sin^2\theta\cos\beta+\sin^2\phi\sin^2\theta\sin\beta)\,E^{o}_{\parallel}+\sin\phi\cos\theta\sin\theta\,E^{o}_{\perp}, \tag{9}$$

$$\mu_z=(\cos\phi\cos\theta\sin\theta\cos\beta+\sin\phi\cos\theta\sin\theta\sin\beta)\,E^{o}_{\parallel}+\cos^2\theta\,E^{o}_{\perp}. \tag{10}$$

The field $\mathbf{E}(\mathbf{r}',\omega)$ that interacts with the 2D system can be approximated as[29]

$$\mathbf{E}(\mathbf{r}',\omega)\approx\mathbf{E}^{o}(\mathbf{r}',\omega)+\frac{\omega^2}{\varepsilon_o c^2}\,\overleftrightarrow{\mathbf{G}}^{o}(\mathbf{r},\mathbf{r}';\omega)\,\boldsymbol{\mu}(\mathbf{r},\omega), \tag{11}$$

where c is the vacuum speed of light and $\overleftrightarrow{\mathbf{G}}^{o}$ is the free-space dyadic Green's function in the absence of tip.[30] We reject in our analysis the incident laser field $\mathbf{E}^{o}(\mathbf{r}',\omega)$ in Eq. (11) since the local field due to the metal tip is much stronger in the vicinity of the tip. In a Cartesian system, $\overleftrightarrow{\mathbf{G}}^{o}(\mathbf{r},\mathbf{r}';\omega)$ is defined as[30]

$$\overleftrightarrow{\mathbf{G}}^{o}(\mathbf{r},\mathbf{r}';\omega)=\frac{e^{ikR}}{4\pi R}\left[\left(1+\frac{ikR-1}{k^2R^2}\right)\overleftrightarrow{\mathbf{I}}+\frac{3-3ikR-k^2R^2}{k^2R^2}\frac{\mathbf{RR}}{R^2}\right], \tag{12}$$

where $k = \omega/c$ is the modulus of the wave vector of the electromagnetic field in the free space, $\overleftrightarrow{\mathbf{I}}$ is the unity dyad, R is the absolute value of the vector $\mathbf{R} = \mathbf{r} - \mathbf{r}'$, and $\mathbf{RR}$ is the outer product of $\mathbf{R}$ with itself. The Green's function $\overleftrightarrow{\mathbf{G}}^{\mathrm{o}}(\mathbf{r},\mathbf{r}';\omega)$ given in Eq. (12) has terms in $(kR)^{-1}$, $(kR)^{-2}$, and $(kR)^{-3}$. In the near-field, for which $R \ll \lambda$, with $\lambda = 2\pi/k$, only the terms proportional to $(kR)^{-3}$ survive. In this case, the near-field term of the free-space dyadic Green's function can be derived from Eq. (12) as[30]

$$\overleftrightarrow{\mathbf{G}}^{\mathrm{o}}_{\mathrm{NF}}(\mathbf{r},\mathbf{r}';\omega) = \frac{e^{ikR}}{4\pi k^2 R^3}\left[-\overleftrightarrow{\mathbf{I}} + \frac{3\mathbf{RR}}{R^2}\right]. \tag{13}$$

The Raman dipole generated at the sample defined in Eq. (1) can now be evaluated as

$$\mathbf{p}(\mathbf{r}',\omega_{\mathrm{s}}) = \frac{\omega^2}{\varepsilon_{\mathrm{o}}c^2}\left[2\pi\varepsilon_{\mathrm{o}}\rho_{\mathrm{tip}}^3 f_{\mathrm{e}}(\omega)\right]\begin{bmatrix}\alpha_{11}(G^{\circ}_{xx}\mu_x + G^{\circ}_{xy}\mu_y + G^{\circ}_{xz}\mu_z) + \alpha_{12}(G^{\circ}_{yx}\mu_x + G^{\circ}_{yy}\mu_y + G^{\circ}_{yz}\mu_z)\\ \alpha_{21}(G^{\circ}_{xx}\mu_x + G^{\circ}_{xy}\mu_y + G^{\circ}_{xz}\mu_z) + \alpha_{22}(G^{\circ}_{yx}\mu_x + G^{\circ}_{yy}\mu_y + G^{\circ}_{yz}\mu_z)0\end{bmatrix}, \tag{14}$$

where G^{o}_{ij} are tensor components of the near-field term of the free-space dyadic Green's function given in Eq. (13). This Raman dipole will generate a scattered field at frequency ω_{s}, which, in turn, will generate an induced dipole at the tip apex. The field that reaches the tip for this induction process can be evaluated as

$$\mathbf{E}(\mathbf{r},\mathbf{r}',\omega_{\mathrm{s}}) = \frac{\omega^2}{\varepsilon_{\mathrm{o}}c^2}\,\overleftrightarrow{\mathbf{G}}^{\mathrm{o}}_{\mathrm{NF}}(\mathbf{r}',\mathbf{r};\omega_s)\,\mathbf{p}(\mathbf{r}',\omega_{\mathrm{s}}), \tag{15}$$

and the Raman scattered field at the tip apex is obtained by the product

$$\mathbf{E}_{\mathrm{S}}(\mathbf{r},\mathbf{r}',\omega_{\mathrm{s}}) = \overleftrightarrow{\boldsymbol{\alpha}}_{\mathrm{tip}}\,\mathbf{E}(\mathbf{r},\mathbf{r}',\omega_{\mathrm{s}}). \tag{16}$$

III. INTENSITY OF THE SCATTERED SIGNAL IN THE NEAR-FIELD REGIME

In this section we proceed with the calculation of the intensity of the Raman scattered signal that reaches the detector at $\mathbf{r}_{\mathrm{o}}$ (see Fig. 1). On length scales smaller than the phonon coherence length (L_{ph}) the Raman dipoles described in Eq. (15) add coherently (see complete discussion about the spatial coherence properties of TERS in the supplemental material of Ref. 26). Therefore, it is necessary to account for the coherence properties of the dipole distribution $\mathbf{p}(\mathbf{r}',\omega_{\mathrm{s}})$ in Eq. (16). As discussed in Ref. 26, for strongly localized light sources such as near-field optical probes, we have to account for the detection of coherent phonons, since the phonon coherence length can assume values on the same magnitude order of ρ_{tip} ($\sim$10 nm).[31] In this case, the intensity of the near-field Raman scattered signal can be evaluated as

$$I^{\mathrm{Coh}}_{\mathrm{NF}}(\mathbf{r}_{\mathrm{o}},\omega_s) \propto \left|\int_{-\infty}^{+\infty}\int_{-\infty}^{+\infty} dx'\,dy'\mathbf{E}_{\mathrm{S}}(\mathbf{r},\mathbf{r}',\omega_{\mathrm{s}})\right|^2, \tag{17}$$

where we neglected any phase differences between surface elements. This approximation is justified considering that the tip field is spatially localized to a length scale much smaller than the wavelength of Raman scattered light. Evaluation of the above integral gives the near-field Raman intensity in the coherent case

$$\begin{aligned} I^{\mathrm{Coh}}_{\mathrm{NF}}&(\mathbf{r}_{\mathrm{o}},\omega_s)\\ &\propto \frac{\rho_{\mathrm{tip}}^{12}\,|f_{\mathrm{e}}(\omega)\,f_{\mathrm{e}}(\omega_{\mathrm{s}})|^2}{(\Delta+\rho_{\mathrm{tip}})^8}\,[E^{\circ}_{\parallel}\cos(\phi-\beta)\sin\theta + E^{\circ}_{\perp}\cos\theta]^2\\ &\times\{16\cos^2\theta(\alpha_{11}+\alpha_{22})^2 + \sin^2\theta[\cos\phi(3\alpha_{11}+\alpha_{22})\\ &+\sin\phi(\alpha_{12}+\alpha_{21})]^2 + \sin^2\theta[\sin\phi(\alpha_{11}+3\alpha_{22})\\ &+\cos\phi(\alpha_{12}+\alpha_{21})]^2\}. \end{aligned} \tag{18}$$

In the case where the interaction length is larger than the phonon coherence length L_{ph}, there is no phase correlation between the dipoles and, hence, the partial fields at the detector add incoherently. In this case the Raman scattered intensity assumes the form

$$I^{\mathrm{Incoh}}_{\mathrm{NF}}(\mathbf{r}_{\mathrm{o}},\omega_s) \propto \int_{-\infty}^{+\infty}\int_{-\infty}^{+\infty} dx'\,dy'|\mathbf{E}_{\mathrm{S}}(\mathbf{r},\mathbf{r}',\omega_{\mathrm{s}})|^2, \tag{19}$$

whose direct evaluation leads to

$$\begin{aligned} I^{\mathrm{Incoh}}_{\mathrm{NF}}(\mathbf{r}_{\mathrm{o}},\omega_s) \propto\ & \frac{\rho_{\mathrm{tip}}^{12}|f_{\mathrm{e}}(\omega)f_{\mathrm{e}}(\omega_{\mathrm{s}})|^2}{(\Delta+\rho_{\mathrm{tip}})^{10}}[E^{\circ}_{\parallel}\cos(\phi-\beta)\sin\theta + E^{\circ}_{\perp}\cos\theta]^2\big\{[79+38\cos(2\theta)+3\cos(4\theta)]\big[(\alpha_{11}+\alpha_{22})^2+(\alpha_{12}+\alpha_{21})^2\\ &+2\big(\alpha_{11}^2+\alpha_{22}^2\big)\big] + 33\cos(4\phi)(\sin^4\theta-3/8)[(\alpha_{11}-\alpha_{22})^2-(\alpha_{12}+\alpha_{21})^2]\\ &+6\sin^2\theta[33+7\cos(2\theta)]\big[\cos(2\phi)\big(\alpha_{11}^2-\alpha_{22}^2\big)+\sin(2\phi)(\alpha_{11}+\alpha_{22})(\alpha_{12}+\alpha_{21})\big]\\ &+66\sin(4\phi)\sin^4\theta(\alpha_{11}-\alpha_{22})(\alpha_{12}+\alpha_{21})\big\}. \end{aligned} \tag{20}$$

TABLE I. Summary for the tip-sample distance dependence of the near-field Raman intensity (I_{NF}) in 0D, 1D, and 2D systems. The numbers are the powers ℓ at $I_{NF} \propto (\Delta + \rho_{tip})^{\ell}$.

	0D	1D	2D
Coherent	−12	−10	−8
Incoherent	−12	−11	−10

The interaction length is roughly defined by the tip radius ρ_{tip} and hence we are in the coherent case if $L_{ph} \gg \rho_{tip}$ and in the incoherent case if $L_{ph} \ll \rho_{tip}$. If L_{ph} is on the order of ρ_{tip} we have to consider partial coherence. Notice that in both cases, coherent and incoherent, the scattered intensity is proportional to the 4th power of the enhancement factor [assuming $f_e(\omega) \approx f_e(\omega_s)$].[20,21,26] However, there is a remarkable difference between the two cases. While in the coherent case the intensity scales as $(\Delta + \rho_{tip})^{-8}$, in the incoherent case it goes with $(\Delta + \rho_{tip})^{-10}$. The latter is in agreement with the analysis performed in Refs. 24 and 27, which only considered the incoherent case.

We have shown in a previous work that the near-field Raman signal originated from 1D systems scales as $(\Delta + \rho_{tip})^{-10}$ and $(\Delta + \rho_{tip})^{-11}$ for the coherent and incoherent scattering regimes, respectively.[26] These results are different from the results given in Eqs. (18) and (20) for 2D systems, and show that the tip-sample distance dependence of the near-field scattering intensity is steeper for 1D systems than for 2D systems. This difference is due to the larger cross-sectional area of the 2D system when interacting with the secondary field generated at the tip apex [$\mathbf{E}(\mathbf{r}',\omega)$ given in Eq. (11)]. Let us illustrate this by considering the special case where the tip is vertically aligned ($\theta = 0$ in Fig. 1). If the tip-sample distance is increased (decreased), the magnitude of $\mathbf{E}(\mathbf{r}',\omega)$ will decrease (increase), and this variation will be maximum at $r' = 0$ (position right under the tip). Because the integral sum that determines the scattered intensity runs over the whole sample [Eqs. (17) and (19) for the coherent and incoherent cases, respectively], the scattered field originated from $r' = 0$ (position with maximum $|\partial E(\mathbf{r}',\omega)/\partial z'|$) is more representative in 1D systems than in 2D systems, which explains why the tip-sample distance dependence of the near-field scattering intensity is steeper in the former. Notice that for (quasi) 0D systems such as quantum dots or single molecules, the tip-sample dependence is even steeper, scaling with $(\Delta + \rho_{tip})^{-12}$ as predicted for two interacting point-dipoles. Table I summarizes the tip-sample distance dependence of the near-field Raman intensity in 0D, 1D, and 2D systems, considering both coherent and incoherent scattering regimes.

IV. PRACTICAL CONSIDERATIONS FOR VIBRATIONAL MODES IN GRAPHENE AND BN

In this section, we apply our theory to the E_{2g} vibrational mode occurring in graphene (symmorphic space group D^1_{6h}) and monolayer BN (symmorphic space group D^1_{3h}).[32] It comes from the two-degenerated bond stretching vibration involving two neighbor atoms, giving rise to the G band in graphene ($\sim$1584 cm^{-1}) and BN ($\sim$1366 cm^{-1}). The associated Raman polarizability tensors (namely, E_{2g_1} and E_{2g_2}) have the form[33]

$$\overleftrightarrow{\boldsymbol{\alpha}}^{R}(E_{2g_1}) = \begin{bmatrix} 1 & 0 & 0 \\ 0 & -1 & 0 \\ 0 & 0 & 0 \end{bmatrix}, \quad \text{and}$$

$$\overleftrightarrow{\boldsymbol{\alpha}}^{R}(E_{2g_2}) = \begin{bmatrix} 0 & 1 & 0 \\ 1 & 0 & 0 \\ 0 & 0 & 0 \end{bmatrix}. \tag{21}$$

For the coherent case, substitution of the matrix elements of the polarizability tensors $\overleftrightarrow{\boldsymbol{\alpha}}^{R}(E_{2g_1})$ and $\overleftrightarrow{\boldsymbol{\alpha}}^{R}(E_{2g_2})$ [Eq. (21)] in Eq. (18) gives

$$I^{Coh}_{NF}(E_{2g_1}) = I^{Coh}_{NF}(E_{2g_2}) \propto \frac{\rho^{12}_{tip} f^4_e(\omega)}{(\Delta + \rho_{tip})^8} \sin^2\theta \times [E^{\circ}_{\parallel}\cos(\phi - \beta)\sin\theta + E^{\circ}_{\perp}\cos\theta]^2. \tag{22}$$

For the incoherent case, substitution of the matrix elements of the polarizability tensors $\overleftrightarrow{\boldsymbol{\alpha}}^{R}(E_{2g_1})$ and $\overleftrightarrow{\boldsymbol{\alpha}}^{R}(E_{2g_2})$ [Eq. (21)] in Eq. (20) yield, respectively,

$$I^{Incoh}_{NF}(E_{2g_1}) \propto \frac{\rho^{12}_{tip} f^4_e(\omega)}{(\Delta + \rho_{tip})^{10}} [E^{\circ}_{\parallel}\cos(\phi - \beta)\sin\theta + E^{\circ}_{\perp}\cos\theta]^2 \times \{[79 + 38\cos(2\theta) + 3\cos(4\theta)] + 33\cos(4\phi) \times (\sin^4\theta - 3/8)\}, \tag{23}$$

and

$$I^{Incoh}_{NF}(E_{2g_2}) \propto \frac{\rho^{12}_{tip} f^4_e(\omega)}{(\Delta + \rho_{tip})^{10}} [E^{\circ}_{\parallel}\cos(\phi - \beta)\sin\theta + E^{\circ}_{\perp}\cos\theta]^2 \times \{[79 + 38\cos(2\theta) + 3\cos(4\theta)] - 33\cos(4\phi) (\sin^4\theta - 3/8)\}. \tag{24}$$

The total intensity in the incoherent case is obtained by the sum of the two contributions:

$$I^{Incoh}_{NF}(E_{2g_1}) + I^{Incoh}_{NF}(E_{2g_2}) \propto \frac{\rho^{12}_{tip} f^4_e(\omega)}{(\Delta + \rho_{tip})^{10}} [E^{\circ}_{\parallel}\cos(\phi - \beta)\sin\theta + E^{\circ}_{\perp}\cos\theta]^2 \times [79 + 38\cos(2\theta) + 3\cos(4\theta)]. \tag{25}$$

To illustrate our analysis, we consider an incident field which has been strongly focused by a high numeric aperture (NA) objective lens with NA = 1.4, using two possible configurations: a radially symmetric (doughnut) mode and a linearly polarized mode. In the case of a radially polarized mode, the amplitude of the longitudinal component of the incident electric field located at the center of the focus area is about two times larger than the amplitude of the radial component of the incident field, that is, $E^{\circ}_{\perp} \simeq 2E^{\circ}_{\parallel}$.[30] For linearly polarized beams, there are two longitudinal field lobes slightly displaced from the center of the beam, characteristic for strongly focused Gaussian beams, and in this case the amplitude of the longitudinal field component is about three times smaller than the amplitude of the linear component, that is, $E^{\circ}_{\perp} \simeq (1/3)E^{\circ}_{\parallel}$.[30]

Figures 2(a) and 2(b) show two-dimensional plots of the incoherent near-field Raman intensity related to the E_{2g_1} and E_{2g_2} vibrational modes, respectively, as a function of ϕ and β (see Fig. 1 for reference). The plots were obtained from Eqs. (23) and (24), respectively, considering $\theta = 45^{\circ}$, and

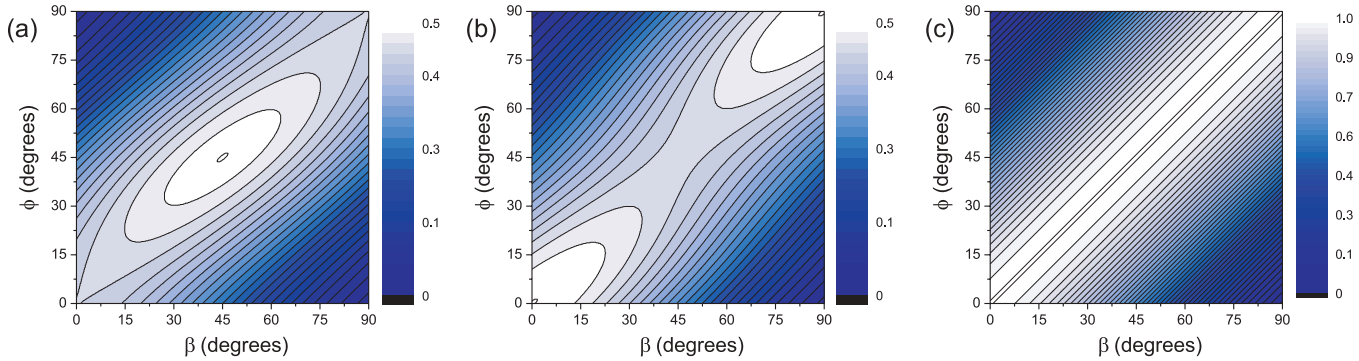

FIG. 2. (Color online) (a),(b) Two-dimensional plots of of the incoherent near-field Raman intensity related to the E_{2g_1} and E_{2g_2} vibrational modes, respectively, as a function of ϕ and β (see Fig. 1 for reference). The plots were obtained from Eqs. (23) and (24), respectively, considering $\theta = 45^\circ$, and a linearly polarized incident laser beam. (c) Total scattered intensity of the G mode $[I_{NF}^{Incoh}(E_{2g}) = I_{NF}^{Incoh}(E_{2g_1}) + I_{NF}^{Incoh}(E_{2g_2})]$ under the same conditions considered in panels (a) and (b).

a linearly polarized incident laser beam. As shown in panel (a), $I_{NF}^{Incoh}(E_{2g_1})$ presents a maximum value for $\phi = \beta = 45^\circ$, and minima for $|\phi - \beta| = 90^\circ$. For $I_{NF}^{Incoh}(E_{2g_1})$ [panel (b)], the maxima occur for $\phi = \beta = 0^\circ$ and $\phi = \beta = 90^\circ$, and the minima occur for $|\phi - \beta| = 90^\circ$. Figure 2(c) shows the total scattered intensity of the G mode $[I_{NF}^{Incoh}(E_{2g}) = I_{NF}^{Incoh}(E_{2g_1}) + I_{NF}^{Incoh}(E_{2g_2})]$ under the same conditions considered in panels (a) and (b) (linearly polarized incident beam, $\theta = 45^\circ$). As depicted in Fig. 2(c), the maximum total scattering intensity is achieved whenever the polarization of the parallel component of the incident field is aligned with the projection of the tip shaft on the x-y plane, that is, whenever the condition $\phi = \beta$ is achieved. This result is a consequence of the fact that the total scattering intensity of the twofold degenerated E_{2g} mode is isotropic in the x-y plane. Notice that for a radially polarized laser beam, the condition $\phi = \beta$ is always achieved, since the radial component of the incident field is also isotropic in the x-y plane. The 2D plot of the intensity of the coherent near-field Raman signal related to the E_{2g_1} and E_{2g_2} vibrational modes as a function of ϕ and β give a similar result as shown in Fig. 2(c) and is not reproduced here.

Figure 3(a) shows the plot of the total incoherent scattered intensity of the G mode $[I_{NF}^{Incoh}(E_{2g}) = I_{NF}^{Incoh}(E_{2g_1}) + I_{NF}^{Incoh}(E_{2g_2})]$ as a function of θ, for $\phi = \beta$. The solid (blue) and dashed (red) lines were obtained considering radially and linearly polarized laser modes, respectively. For the radially polarized mode, the scattered intensity is clearly higher for low θ angles (tip vertically positioned), being maximum at $\theta \simeq 15^\circ$, and minimum (but not null) at $\theta \simeq 90^\circ$ (tip horizontally positioned). For the linearly polarized mode, the condition for the maximum scattered intensity is achieved for $\theta \simeq 45^\circ$. However, it is clear from the figure that even in this case the near-field signal intensity is much higher (about ten times) if the radially polarized laser mode is applied. Figure 3(b) shows the same analysis the for total coherent scattered intensity $[I_{NF}^{coh}(E_{2g})]$. For the radially polarized mode, the scattered intensity reaches the maximum value at $\theta \simeq 60^\circ$, while for the linearly polarized mode the maximum scattered intensity is achieved for $\theta \simeq 80^\circ$. The maximum value for the scattered intensity is considerably higher for the radially polarized laser mode. In both cases (radially and linearly polarized laser modes), the coherent scattered intensity is null

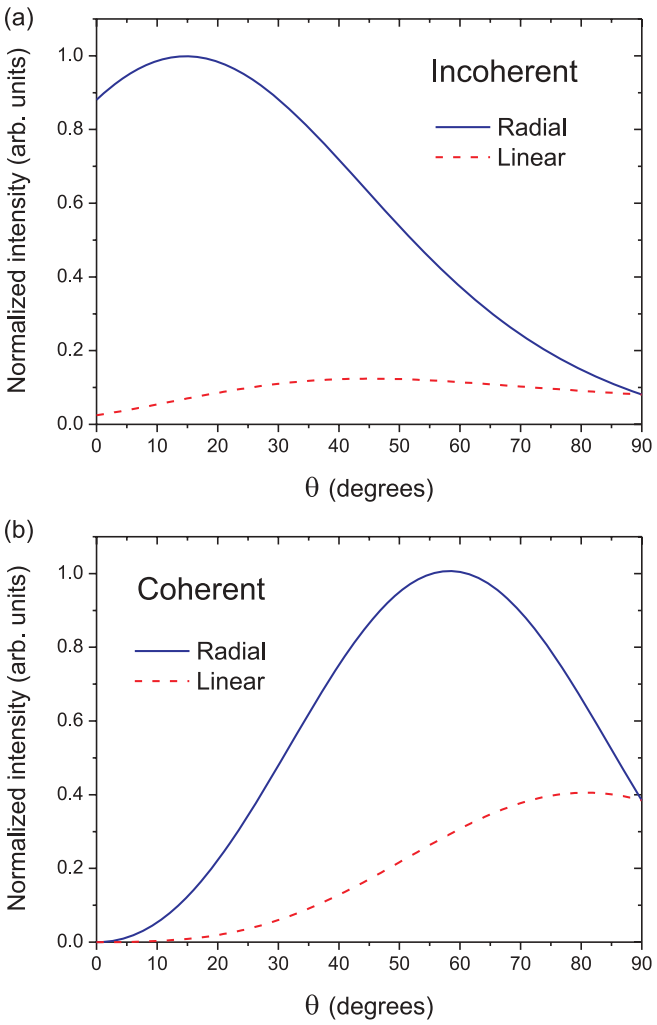

FIG. 3. (Color online) (a) Total incoherent scattered intensity of the G mode $[I_{NF}^{Incoh}(E_{2g}) = I_{NF}^{Incoh}(E_{2g_1}) + I_{NF}^{Incoh}(E_{2g_2})]$ as a function of θ, for $\phi = \beta$. The solid (blue) and dashed (red) lines were obtained considering radially and linearly polarized laser modes, respectively. (b) Same analysis the for total coherent scattered intensity $[I_{NF}^{coh}(E_{2g})]$.

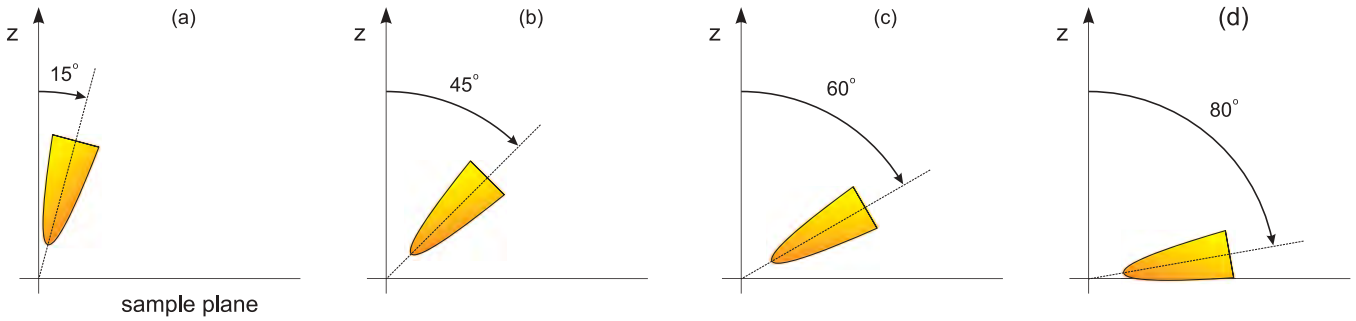

FIG. 4. (Color online) Optimal values for the tip inclination (angle θ) in the following configurations: (a) E_{2g} mode, incoherent scattering, radially polarized laser beam; A_{1g} mode, incoherent and coherent scattering, radially polarized laser beam; (b) E_{2g} mode, incoherent scattering, linearly polarized laser beam; A_{1g} mode, incoherent and coherent scattering, linearly polarized laser beam; (c) E_{2g} mode, coherent scattering, radially polarized laser beam; (d) E_{2g} mode, coherent scattering, linearly polarized laser beam.

for $\theta = 0$ due to interference effects [notice the $\sin^2\theta$ term in Eq. (22)].

We also analyzed the totally symmetric A_{1g} vibrational mode occurring at the corner of the first Brillouin zone of 2D hexagonal systems with D^1_{6h} symmetry. This mode is specially important in graphene, since it gives rise to the defect-induced D band occurring at $\sim$1350 cm^{-1}, and also to the two-phonon associated G' (also called 2D) band occurring at $\sim$2700 cm^{-1} (Ref. 15). The results for both cases, incoherent and coherent, are very similar to the result shown in Fig. 3(a), which account for the total near-field intensity originated from the E_{2g} mode in the incoherent regime. Notice that the interference effects that annul the coherent scattered intensity originated from the E_{2g} mode for $\theta = 0$ no longer take place for the A_{1g} mode. This difference provides a reliable way to distinguish the coherent signal from the incoherent signal in graphene, since the detection of a lower enhancement factor for the G band (E_{2g} mode) when compared to the G' band (A_{1g} mode) at low values of θ (tip vertically aligned) would indicate the predominance of the coherent regime.

It should be emphasized that, except when the tip is horizontally aligned ($\theta = 90°$), the near-field intensity obtained by using a radially polarized incident laser beam is generally more intense than when a linearly polarized laser beam is applied (see Fig. 3). The reason for this difference is the ratio between the amplitudes of the longitudinal and parallel components of the incident field in both cases. As pointed out at the beginning of this section, while for radially polarized modes the amplitude of the longitudinal component of the electric field is two times larger than the amplitude of its parallel component, for linearly polarized modes the former is three times smaller. Notice that for incoherent scattering, the near-field intensity obtained with the tip vertically aligned ($\theta = 0$) is about 20 times larger for radially polarized laser beams than for linearly polarized laser beams [see Fig. 3(a)]. Although the calculations here are performed for 2D systems, this remarkable difference is in agreement with previous TERS experiments in carbon nanotubes.[21]

V. QUANTITATIVE ANALYSIS

The relative enhancement between the Raman signals generated in the near-field and far-field regimes can be defined as

$$\frac{I_{NF}}{I_{FF}} = \gamma \frac{A_{NF}}{A_{FF}}, \tag{26}$$

where I_{NF} and I_{FF} denote the measured Raman intensities in the near-field and far-field regimes, respectively, A_{NF} and A_{FF} are the sample areas probed in the near-field and far-field regimes, respectively, and γ is an effective enhancement factor. While A_{FF} is the entire area illuminated by the incident laser, A_{NF} is the area under the tip. Typical values for the laser focus diameter and the tip diameter are 300 nm (considering an objective lens with NA = 1.4 and excitation field in the optical range) and 20 nm, respectively. The enhancement factor strongly depends on the tip properties, and previous experiments performed in carbon nanotubes have shown that γ values up to 240 can be obtained for gold tips using radially polarized laser modes.[26] Taking into account these values of A_{NF}, A_{FF}, and γ, we can estimate a relative enhancement I_{NF}/I_{FF} for the G band in graphene and monolayer BN which is close to 1.

In recent Raman studies of Ar$^+$-bombarded graphene, we showed experimentally that the ratio between the intensities of the D and G bands (I_D/I_G) is linearly proportional to the point defect density (n_D) generated by the impact of the ions on the graphene plane.[14,15] The proportionality constant strongly depends on the wavelength of the incident laser used in the experiment, and for a typical 632.8-nm He-Ne laser we have $I_D/I_G \simeq 10^3\ \text{nm}^2 \times n_D$.[15] According to this relation (valid for far field regime), a single point defect in the focus area ($n_D \sim 3.5 \times 10^{-6}\text{nm}^{-2}$) would generate a D band signal about 300 times weaker than the G band signal, which makes the Raman study of a single point defect a difficult task in far-field conditions. However, the situation can be quite different for near-field experiments because the D-band scattering process takes place in an area of $\sim$10 nm^2 surrounding the point defect.[14,15] Since this area is much smaller than the usual tip apex area ($\sim 10^3$ nm^2), the relative enhancement for the D-band scattering generated by a single point defect will be equal to the absolute enhancement factor γ. Therefore, for a near-field experiment using a tip with $\gamma \sim 240$, the D-band signal originated from a single point defect would have the same magnitude order as the G-band signal originated from the whole focus area, making possible the study of local features

that breaks the translational symmetry such as vacancies,[34] adatoms,[35] or topological defects.[36]

VI. CONCLUSIONS

In summary, we have developed a general theory that describes the near-field Raman enhancement in 2D systems. We derived two master equations [Eqs. (18) and (20)] which describe the near-field Raman intensity as a function of the tip-sample distance, Raman polarizability tensor components, incident laser beam configuration, and tip orientation relative to the sample plane. The analysis takes into account both spatially incoherent and coherent scattering regimes. While in the incoherent case the intensity is proportional to the 10th power of the tip-sample distance (in agreement with previous calculations presented in Refs. 24 and 27), in the coherent case it goes with the 8th power. In both cases the near-field signal is proportional to the 4th power of the field enhancement factor f_e. We analyzed the results for vibrational modes occurring in graphene and monolayer BN, taking into account both radially polarized and linearly polarized incident laser beams. The optimal conditions for the tip inclination angle θ for different configurations were determined, and the results are summarized in Fig. 4. Numerical analysis based on previous TERS experiments performed in 1D systems shows that spatially localized features smaller than the tip diameter in 2D systems can generate a near-field Raman signal whose intensity is comparable to the intensity of the far-field Raman signal obtained from the whole area illuminated by the incident laser. All these parameters together provide a guide for TERS experiments in 2D systems and can be extended to opaque bulk materials with flat surfaces.

ACKNOWLEDGMENTS

This work was supported by the Rede Brasileira de Pesquisa e Instrumentação em Nano-Espectroscopia Óptica-MCT. R.M., A.J., and L.G.C. acknowledge the support from the Brazilian agencies CNPq and FAPEMIG. L.N. and R.B. acknowledge the support from US Department of Energy (Grant No. DE-FG02-05ER46207).

*cancado@fisica.ufmg.br

[1] K. S. Novoselov, A. K. Geim, S. V. Morozov, D. Jiang, M. I. Katsnelson, I. V. Grigorieva, D. V. Dubonos, and A. A. Firsov, Nature (London) **438**, 197 (2005).
[2] Y. Zhang, Y.-W. Tan, H. L. Stormer, and P. Kim, Nature (London) **438**, 201 (2005).
[3] A. H. Castro Neto and K. Novoselov, Rep. Prog. Phys. **74**, 082501 (2011).
[4] X. Du, I. Skachko, F. Duerr, A. Luican, and E. Y. Andrei, Nature (London) **462**, 192 (2009).
[5] C. R. Dean, A. F. Young, I. Meric, C. Lee, L. Wang, S. Sorgenfrei, K. Watanabe, T. Taniguchi, P. Kim, K. L. Shepard, and J. Hone, Nat. Nanotech. **5**, 722 (2010).
[6] Z. Ni, L. Ponomarenko, R. Nair, R. Yang, S. Anissimova, I. Grigorieva, F. Schedin, P. Blake, Z. Shen, E. Hill, K. S. Novoselov, and A. K. Geim, Nano Lett. **10**, 3868 (2010).
[7] L. Liao, Y.-C. Lin, M. Bao, R. Cheng, J. Bai, Y. Liu, Y. Qu, K. L. Wang, Y. Huang, and X. Duan, Nature (Nature) **467**, 305 (2010).
[8] Y. Wu, Y.-M. Lin, A. A. Bol, K. A. Jenkins, F. Xia, D. B. Farmer, Y. Zhu, and Ph. Avouris, Nature (London) **472**, 74 (2011).
[9] Ph. Avouris, Nano Lett. **10**, 4285 (2010).
[10] J. N. Coleman, M. Lotya, A. O' Neill, S. D. Bergin, P. J. King, U. Khan, K. Young, A. Gaucher, S. De, R. J. Smith, I. V. Shvets, S. K. Arora, G. Stanton, H.-Y. Kim, K. Lee, G. T. Kim, G. S. Duesberg, T. Hallam, J. J. Boland, J. J. Wang, J. F. Donegan, J. C. Grunlan, G. Moriarty, A. Shmeliov, R. J. Nicholls, J. M. Perkins, E. M. Grieveson, K. Theuwissen, D. W. McComb, P. D. Nellist, and V. Nicolosi, Science **331**, 568 (2011).
[11] B. Radisavljevic, A. Radenovic, J. Brivio, V. Giacometti, and A. Kis, Nat. Nanotech. **6**, 147 (2011).
[12] R. V. Gorbachev, I. Riaz, R. R. Nair, R. Jalil, L. Britnell, B. D. Belle, E. W. Hill, K. S. Novoselov, K. Watanabe, T. Taniguchi, A. K. Geim, and P. Blake, Small **7**, 465 (2011).
[13] C. Lee, H. Yan, L. E. Brus, T. F. Heinz, J. Hone, and S. Ryu, ACS Nano **4**, 2695 (2010).
[14] M. M. Lucchese, F. Stavale, E. H. Martins Ferriera, C. Vilane, M. V. O. Moutinho, R. B. Capaz, C. A. Achete, and A. Jorio, Carbon **48**, 1592 (2010).
[15] L. G. Cançado, A. Jorio, E. H. Martins Ferreira, F. Stavale, C. A. Achete, R. B. Capaz, M. V. O. Moutinho, A. Lombardo, T. S. Kulmala, and A. C. Ferrari, Nano Lett. **11**, 3190 (2011).
[16] J. H. Chen, W. G. Cullen, C. Jang, M. S. Fuhrer, and E. D. Williams, Phys. Rev. Lett. **102**, 236805 (2009).
[17] F. Guinea, M. I. Katsnelson, and A. K. Geim, Nat. Phys. **6**, 30 (2010).
[18] L. Novotny, Phys. Today **64**, 47 (2011).
[19] N. Hayazawa, A. Tarun, A. Taguchi, and S. Kawata, Jpn. J. Appl. Phys. **48**, 08JA02 (2009).
[20] A. Hartschuh, Angew. Chem. Int. Ed. **47**, 8178 (2008).
[21] L. G. Cançado, A. Hartschuh, and L. Novotny, J. Raman Spectrosc. **40**, 1420 (2009).
[22] S. S. Kharintsev, G. G. Hoffmann, P. S. Dorozhkin, G. de With, and J. Loos, Nanotech **18**, 315502 (2007).
[23] T.-A. Yano, P. Verma, Y. Saito, T. Ichimura, and S. Kawata, Nat. Phot. **3**, 473 (2009).
[24] B. Pettinger, K. F. Domke, D. Zhang, G. Picardi, and R. Schuster, Surf. Sci. **603**, 1341 (2009).
[25] Y. Saito, P. Verma, K. Masui, I. Inouye, and S. Kawata, J. Raman Spectrosc. **40**, 1434 (2009).
[26] L. G. Cançado, A. Jorio, A. Ismach, E. Joselevich, A. Hartschuh, and L. Novotny, Phys. Rev. Lett. **103**, 186101 (2009).
[27] F. Schedin, E. Lidorikis, A. Lombardo, V. G. Kravets, A. K. Geim, A. N. Grigorenko, K. S. Novoselov, and A. C. Ferrari, ACS Nano **4**, 5617 (2010).
[28] A. Bouhelier, M. Beversluis, A. Hartschuh, and L. Novotny, Phys. Rev. Lett. **90**, 013903 (2003).

[29]L. Novotny and S. J. Stranick, Annu. Rev. Phys. Chem. **57**, 303 (2006).
[30]L. Novotny and B. Hecht, *Principles of Nano-optics* (Cambridge University Press, New York, 2006).
[31]D. Song, F. Wang, G. Dukovic, M. Zheng, E. D. Semke, L. E. Brus, and T. F. Heinz, Phys. Rev. Lett. **100**, 225503 (2008).
[32]For BN, this vibrational mode is denominated as E'.
[33]R. Loudon, Adv. Phys. **13**, 423 (1964).
[34]R. Faccio, L. Fernández-Werner, H. Pardo, C. Goyenola, O. N. Ventura, and Álvaro W. Mombrú, J. Phys. Chem. C **114**, 18961 (2010).
[35]A. H. Castro Neto, V. N. Kotov, J. Nilsson, V. M. Pereira, N. M. R. Peres, and B. Uchoa, Solid State Commun. **149**, 1094 (2008).
[36]J. da Silva-Araújo, H. Chacham, and R. W. Nunes, Phys. Rev. B **81**, 193405 (2010).